analytical chemistry

Open Access

This article is licensed under CC-BY-NC-ND 4.0

pubs.acs.org/ac Article

Spatially Resolved Functional Group Analysis of OLED Materials Using EELS and ToF-SIMS

Kyun Seong Dae, Kyoung-Soon Jang, Chang Min Choi,*,∥ and Jae Hyuck Jang*,∥

Cite This: *Anal. Chem.* 2024, 96, 12616−12621

Read Online

ACCESS | Metrics & More | Article Recommendations | Supporting Information

ABSTRACT: Electron energy-loss spectroscopy (EELS) is widely used in analyzing the electronic structure of inorganic materials at high spatial resolution. In this study, we use a monochromator to improve the energy resolution, allowing us to analyze the electronic structure of organic light-emitting diode (OLED) materials with greater precision. This study demonstrates the use of the energy-loss near-edge structure to map the nitrogen content of organic molecules and identify the distinct bonding characteristics of aromatic carbon and pyridinic nitrogen. Furthermore, we integrate EELS with time-of-flight secondary ion mass spectrometry for molecular mapping of three different bilayers composed of OLED materials. This approach allows us to successfully map functional groups in the by-layer OLED and measure the thickness of two OLED layers. This study introduces spatially resolved functional group analysis using electron beam spectroscopy and contributes to the development of methods for complete nanoscale analysis of organic multilayer architectures.

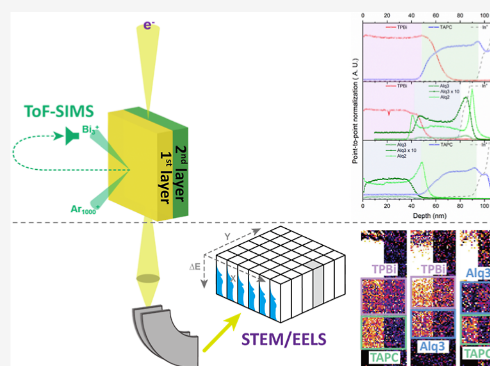

■ INTRODUCTION

Organic light-emitting diodes (OLEDs) have attracted significant interest as lighting sources since their inception by Tang and Vanslyke in 1987.[1] Moreover, their popularity has surged owing to the rapid expansion of the flexible display market, including foldable smartphones, curved monitors, and wearable devices. Significant efforts have been made by academia and industry to enhance the performance of OLEDs, focusing on aspects such as luminance efficiency, color gamut, device stability, and fabrication techniques.[2−4] Improvement in OLED efficiency is achieved by varying the layer thickness, adjusting the dopant concentrations, and employing multilayer structures incorporating various materials for different functionalities.[5−9] These structures include light emission layers and surrounding transport/blocking layers for charge carriers. However, further optimization of OLED performance in competitive lighting sources and displays with desirable standards is still challenging.[10,11] One of the challenges for achieving high performance of OLEDs is the design of an appropriate device architecture that determines the operating voltage and luminance efficiency.[12] Therefore, the multithin-film nanostructures of OLEDs should be assessed to determine the realization of the intended thin-film structure at the desired scale, the generation of internal defect-induced deformation, and changes in the OLED thin layer caused by deterioration.

Therefore, significant efforts have been made to analyze the layered structures of OLEDs. In-chamber ellipsometry (ICE), a type of nondestructive testing, is currently the most widely used method in the production process. Ellipsometry, an optical-based technology, evaluates the dielectric properties, thickness, and uniformity of thin films by measuring the changes in polarization. Moreover, ellipsometry has the advantages of rapid inspection and moderate spatial resolution (a few nanometers); therefore, it is widely used in the evaluation of deposition accuracy (pixel position accuracy). However, owing to the nature of a nondestructive spectrometer such as ICE, it is limited to only one-dimensional structural analysis, and detailed structural feedback, such as failure analysis from defects, is difficult. Another method to verify the structure of an OLED is destructive depth profiling using time-of-flight secondary ion mass spectrometry (ToF-SIMS) with a gas cluster ion beam (GCIB), which is the softest sputtering method currently available for organic materials. Iida et al. suggested that ToF-SIMS depth profiling with tandem mass spectrometry could be used for layer-by-layer analysis of OLEDs.[13] However, while ToF-SIMS depth profiling alone can provide detailed chemical information for each layer as a function of sputter ion dose, sputtering time, or the number of sputtering cycles, it cannot be used to determine the exact thickness of each layer. To determine the actual thickness of each layer, the depth of the crater must be

Received: February 6, 2024
Revised: May 24, 2024
Accepted: June 13, 2024
Published: July 5, 2024

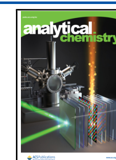

© 2024 The Authors. Published by American Chemical Society

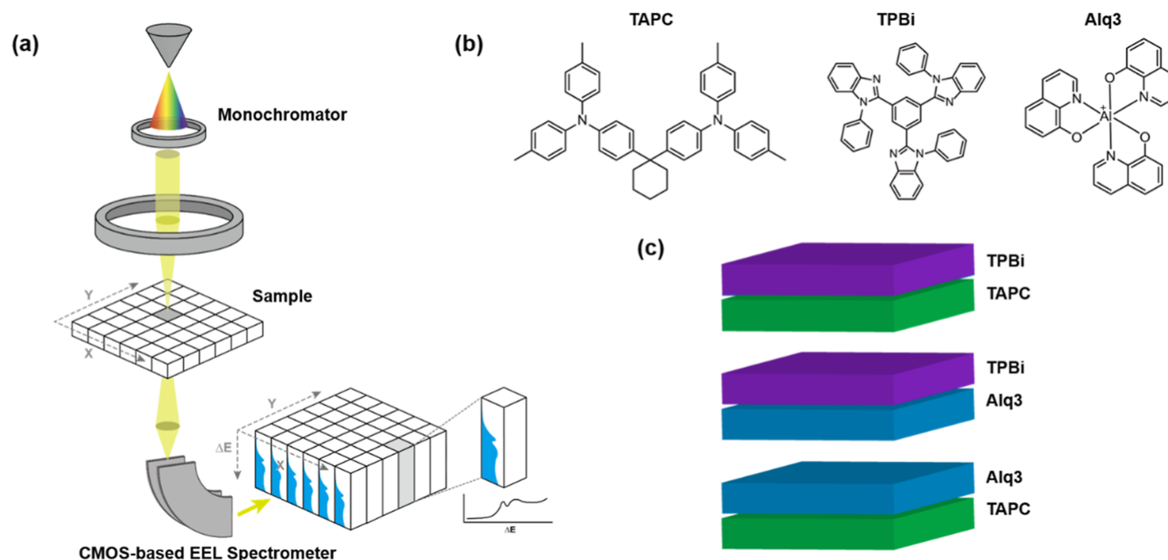

Figure 1. (a) Schematics of STEM/EELS equipment and the method for visualizing ELNES. (b) Organic materials used in OLED for bilayer cross-sectional samples. (c) Illustrations of bilayer architectures alternatively composed of the targeted organic materials.

accurately measured using other equipment after depth profiling and combined with the ToF-SIMS depth profiling results. In addition, the ToF-SIMS depth profiling results might not reflect the exact thickness of each layer as the sputter rate for each material varies slightly depending on the conditions of the sputter ion beam and mixing may also occur between layers due to the sputter ion beam. Therefore, complementary electron microscopy has been continuously developed to analyze cross-sectional structures with a high spatial resolution (approximately a few angstroms). However, transmission electron microscopy (TEM), a conventional imaging method for nanostructure measurements, is not applicable to organic-based semiconductor materials because of the similarity of their components and the subsequent degree of electron scattering.

Graff et al. visualized the nitrogen content in the electron transport layer (ETL), emitting layer (EML), and electron blocking layer (EBL) of a relatively simple blue OLED device by energy-dispersive X-ray spectroscopy (EDS) elemental mapping and TEM and proposed an analysis method for organic thin films.[14] Höfle et al. analyzed OLEDs by visualizing metal oxides in each organic layer using TEM/EDS elemental mapping.[15] Although this elemental mapping may be advantageous in the case of small molecules containing metal atoms or metal oxides, it is limited in the analysis of actual OLEDs, which are composed of thin films of molecules with similar elemental compositions. Molecular-level research, as opposed to atomic-level analysis, will be directly helpful in analyzing the composition/structure of OLEDs and their deterioration process.

Therefore, to thoroughly investigate organic materials, it is necessary to develop a molecular-level analytical method, distinct from conventional approaches, for imaging the chemical bonding characteristics of organic materials. In this study, we analyze nanometer-scale OLEDs using ToF-SIMS, scanning TEM (STEM) analysis offering angstrom-level spatial resolution, and electron energy-loss spectroscopy (EELS), which simultaneously measures the chemical bonding of light elements. This integrated investigative approach combines the advantages of these three methods.

First, we used the two-layer structures of TAPC, TPBi, and Alq3, which are commonly used in OLEDs. Furthermore, we achieved a high spectral resolution capable of distinguishing similar molecular structures using a CMOS-based detector and a monochromated-EELS system. This system can simultaneously improve both energy resolution and signal intensity.

■ EXPERIMENTAL SECTION

Materials. Three organic materials, widely used in OLED devices, were selected for this study: TAPC [$C_{46}H_{46}N_2$; Di-[4-(*N*,*N*-di-*p*-tolyl-amino)-phenyl]cyclohexane], TPBi [$C_{45}H_{30}N_6$; 2,2′,2″-(1,3,5-Benzinetriyl)-tris(1-phenyl-1-H-benzimidazole)], and Alq3 [$C_{27}H_{18}AIN_3O_3$; Tris(8-hydroxyquinolinato) aluminum]. Three different bilayer samples were prepared on indium tin oxide (ITO)-coated glasses using thermal vapor deposition. The materials used in this study were deposited on 20×20 mm^2 ITO-coated glasses in a vacuum of 5.0×10^{-7} Torr at a deposition rate of 0.1 nm/s. The deposition rate was controlled by using a quartz crystal microbalance. Each organic material was deposited to a thickness of 50 nm to produce a double-layer sample with a total thickness of 100 nm. These thin films were ion-milled using a focused ion beam (FIB) until their thickness reached approximately 50 nm.

FIB Preparation. The cross-sectional samples were prepared using the FEI Helios NanoLab DualBeam FIB/SEM system. The initial coarse milling was performed at an acceleration voltage of 30 kV and a beam current of 2.5 nA. For the final thinning process, the voltage was reduced to 5 kV with a beam current of 15 pA to minimize the ion beam damage and remove Ga implantation from the organic materials.

TEM and EELS Experiments. A monochromated ARM-200F (Mono-ARM) operating at 200 kV was used for the acquisition of high-angle annular dark-field (HAADF) and low-angle annular dark-field (LAADF) STEM images, as well as for EELS measurements (spot size 7C). The EELS data were collected using a Gatan imaging filter Continuum HR-1066 spectrometer in dual-EELS mode, with an acquisition time of

https://doi.org/10.1021/acs.analchem.4c00742
Anal. Chem. 2024, 96, 12616−12621

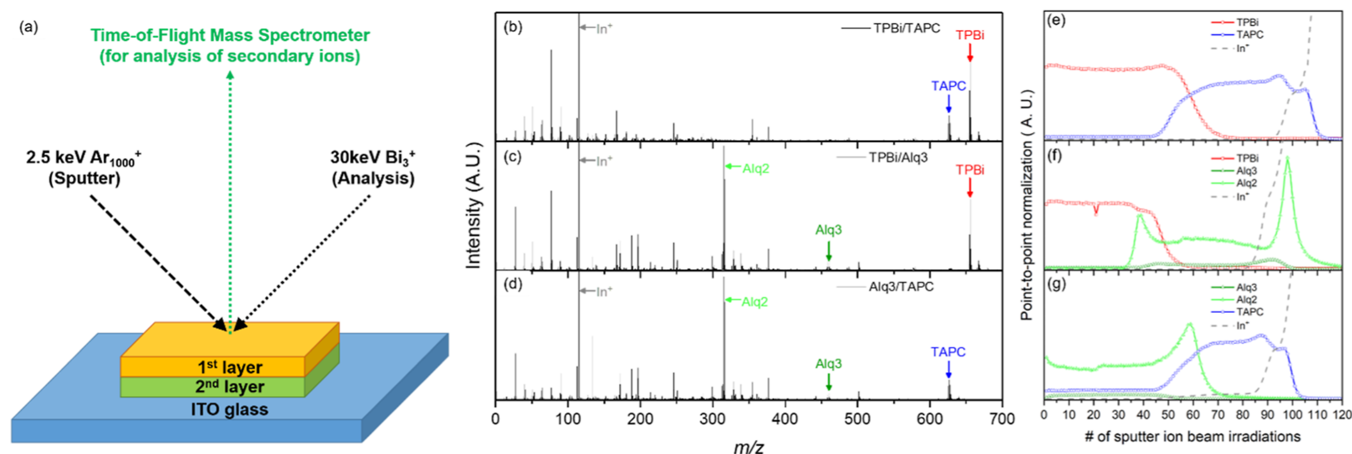

Figure 2. (a) General scheme of ToF-SIMS analysis for organic bilayers. Overall secondary ion mass spectra recorded for (b) TPBi/TAPC, (c) TPBi/Alq3, and (d) Alq3/TAPC. Depth profiles recorded for (e) TPBi/TAPC, (f) TPBi/Alq3, and (g) Alq3/TAPC according to the number of ion beam irradiations sputtered with 2.5 keV Ar_{1000}^+ and analyzed with 30 keV Bi_3^+ projectiles.

0.5 s per spectrum. The convergence semiangle was set to 23.8 mrad, and the collection semiangle was 23 mrad.

To achieve high energy resolution and reduce the irradiated electron current on the organic materials, an energy-selecting slit was employed. For the C−K edge measurements, a dispersion of 0.05 eV/channel and an energy-selecting slit were used, achieving a spectral resolution in the range of 200−210 meV (Figures S1, S3, and S4 and Table S1). The use of the slit reduced the irradiated electron current by approximately 50%, thereby minimizing radiolysis damage while maintaining high spectral resolution. For the N−K edge, a dispersion of 0.15 eV/channel without the energy-selecting slit was adopted due to the necessity of a higher signal-to-noise ratio (SNR) for the nitrogen spectrum (Figure S2).

Further, the alignment and optimization of the STEM for EELS measurements were performed in areas away from the regions of interest to prevent preirradiation damage. Additionally, the electron beam was blanked before and after the EELS measurements to further protect the sample.[16−18]

ToF-SIMS Analysis. SIMS and depth profiling were performed using ToF-SIMS V (IONTOF GmbH, Germany). Secondary ion mass spectra for surface analysis were obtained in the positive mode using a 30 keV Bi_3^+ liquid metal ion beam as the analysis ion gun. For bilayer analysis, depth profiles were obtained using a dual ion beam mode, where a 30 keV Bi_3^+ liquid metal ion beam and a 2.5 keV Ar_{1000}^+ gas cluster ion beam with an etching rate of around 0.33 nm/s were used as the analysis ion gun and the sputter ion gun, respectively. All the depth profiles were obtained using a sputter-ion beam current of approximately 1.0 nA. The sputtered and analyzed areas were squares of dimensions 500 μm × 500 and 200 μm × 200 μm, respectively.

RESULTS AND DISCUSSION

Figure 1 shows a schematic of the STEM/EELS experiment conducted on the three different OLED materials and bilayer thin films. The monochromator significantly improved the energy resolution of EELS to achieve more precise measurements of the atomic bonding structure (Figure S1 and Table S1) compared with the conventional EELS setup; moreover, the CMOS-based electron energy-loss spectrometer exhibited a CMOS processing speed that was sufficiently fast to offset the electron beam reduction caused by the energy slit (Figure 1a).

In particular, the monochromator significantly enhanced the energy resolution to 230 meV, allowing us to distinguish the details of the energy-loss near-edge structure (ELNES) spectra of core loss. However, it simultaneously reduced the electron brightness, leading to a lower SNR. In contrast, the CMOS-based spectrometer exhibited a fast processing speed (>8 kHz) that compensated for the electron beam reduction caused by the energy slit. This allowed us to efficiently collect specific ELNES details for carbon and nitrogen, which can be representative target elements of organic materials.[19] We obtained three-dimensional spectrum images containing the EEL spectra for each two-dimensional pixel. Additionally, Figure 1b,c illustrates the organic bilayer nanostructures consisting of three different OLED materials (TAPC, TPBi, and Alq3) that were targeted for our STEM/EELS and ToF-SIMS analyses. Our results demonstrate the feasibility of using our integrated investigative approach for accurate and precise analysis of the electronic structure of organic materials.

Figure 2b−d shows the secondary ion mass spectra recorded for bilayers alternately composed of organic materials produced by 2.5 keV Ar_{1000}^+ and 30 keV Bi_3^+ ion beam projectiles while measuring the depth profiles. The parent ion signals of the three organic materials (TPBi, TAPC, and Alq3) in these bilayers are shown in Figure 2b−d. Various fragment ions are shown below the parent ion signal of each organic material, and the details of the fragmentation routes are described elsewhere.[20] Unlike TAPC and TPBi, the Alq3 parent ion signal was smaller than the significant main fragment ion signal (m/z 315), which easily lost the hydroxyquinoline ligand.

Figure 2e−g shows the parent ion signals for the three organic materials and the fragment ion signal, Alq2, according to the number of sputter ion beam irradiations. All the depth profiles obtained through ToF-SIMS in the dual ion beam mode were relatively well-separated layer by layer. The depth profiles of TPBi (Figure 2e,f), TAPC (Figure 2e,g), and Alq2 (alq3) (Figure 2f,g) have the same shape as their corresponding substances. Usually, a linear profiler is used to obtain the overall depth of a crater after performing depth profiling of a sample. The total depth of a crater was applied to the data point, providing the thickness of each layer obtained using this method. However, the sputtering rates for each organic material are slightly different during the depth analysis

https://doi.org/10.1021/acs.analchem.4c00742
Anal. Chem. 2024, 96, 12616−12621

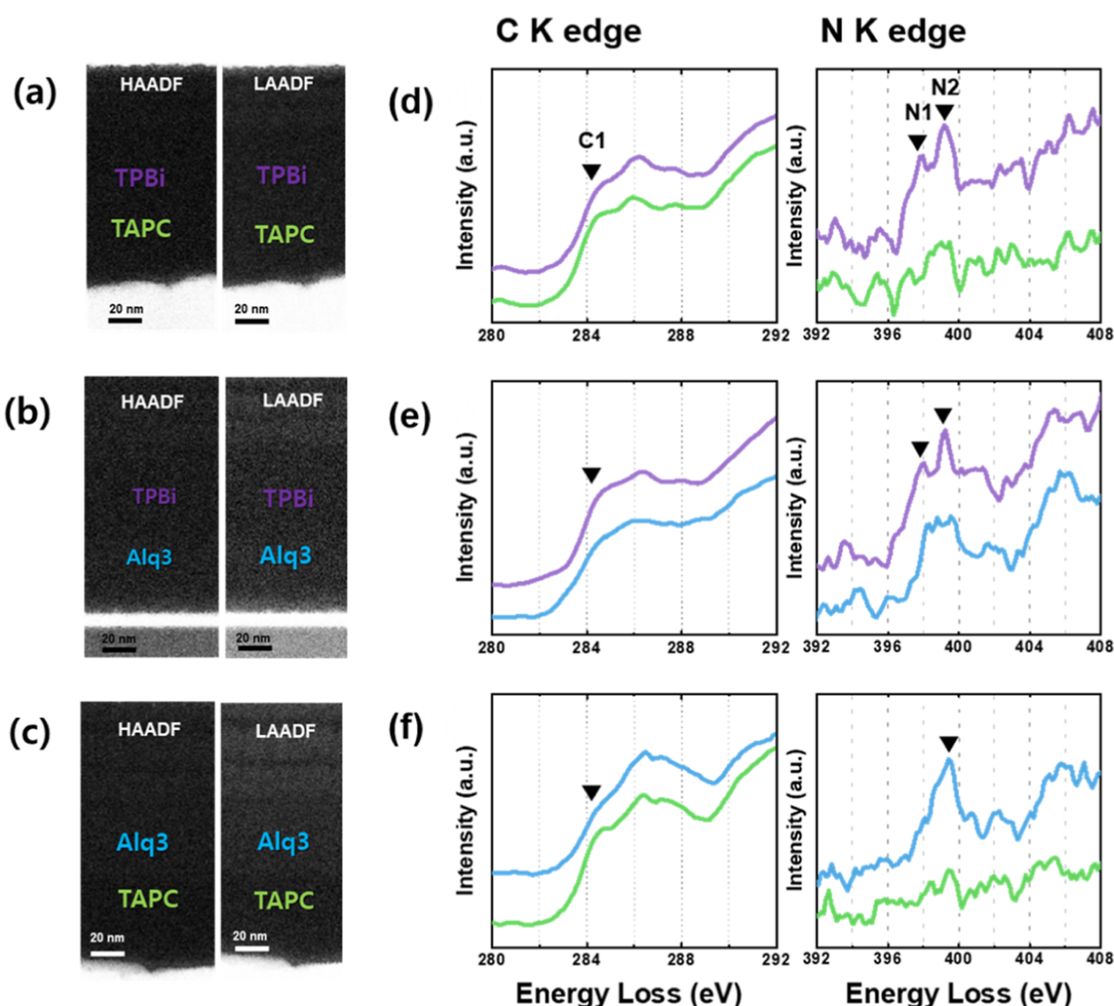

Figure 3. HAADF and LAADF images of organic bilayers for (a) TPBi/TAPC, (b) TPBi/Alq3, and (c) Alq3/TAPC. Corresponding EELS spectra of C K edges and N K edges are shown, illustrating the chemical information for (d) TPBi/TAPC, (e) TPBi/Alq3, and (f) Alq3/TAPC.

using ToF-SIMS, which may provide erroneous depth information for each layer. Even when organic materials are deposited on a substrate with the same thickness, the number of data points is different, indicating that the thickness of each layer may be incorrectly expressed. Therefore, the absolute thickness of each organic layer cannot be measured using ToF-SIMS alone. STEM and monochromated EELS were used to accurately measure the thicknesses of the organic layers.

Figure 3 shows the comparative HAADF and LAADF STEM images (Figure 3a−f) and the corresponding C K and N K edges (Figure 3g−i) acquired for the three organic bilayer films depicted in Figure 1c. In the HAADF images, the Alq3 layer appears slightly brighter than the TPBi and TAPC layers, with contrast differences further enhanced in the LAADF images. However, the TPBi and TAPC layers are not distinguishable using STEM imaging alone. The characteristic spectral peaks from the C K and N K EELS spectra in Figure 3g−i can differentiate the chemical information on each organic film, including elemental composition and chemical bonding states.

The intensity variation of the carbon and nitrogen core loss spectra followed the compositional trends of each layer. That is, the similar intensities of the C K edges indicate similar carbon contents among the three different organic films. The TAPC film showed the lowest nitrogen intensity, indicating that the nitrogen content of the TAPC film was significantly lower than that of the other organic films (Figure 3d−f). However, a complete characterization is inadequate if the nitrogen concentrations of TPBi and Alq3 are similar, as shown in Figure 3e. Therefore, more sophisticated local investigation methods are necessary, such as local probing of the chemical bonds between different chemical species and mapping of these chemical bonds.

To extract bonding maps from spectrum imaging (SI), we use the monochromated ELNES as "fingerprints" for different bonding configurations of a particular species. Using enhanced energy resolution, the C K and N K edges directly exhibited subtle differences in bonding between carbon and nitrogen in the OLED.

The C1 (284 eV) and N1 (398 eV) signals, indicated by the black arrows in Figure 3d−f, were selected as the characteristic bonding states of carbon and nitrogen, respectively. The C1 signal implied an aromatic benzenoid carbon.[21−23] In the case of TAPC, the C1 peak appeared clearly compared to those of the TPBi and Alq3 films (green line in Figure 3d,e). The shape of the C K edge was also clearly different for the three OLED films. Therefore, mono-EELS could be used to distinguish and measure the various carbon bonds in TPBi, Alq3, and TAPC.

We also investigated the nitrogen bonding of OLED films using the N K edge. For TPBi, two N1 and N2 peaks were

https://doi.org/10.1021/acs.analchem.4c00742
Anal. Chem. 2024, 96, 12616−12621

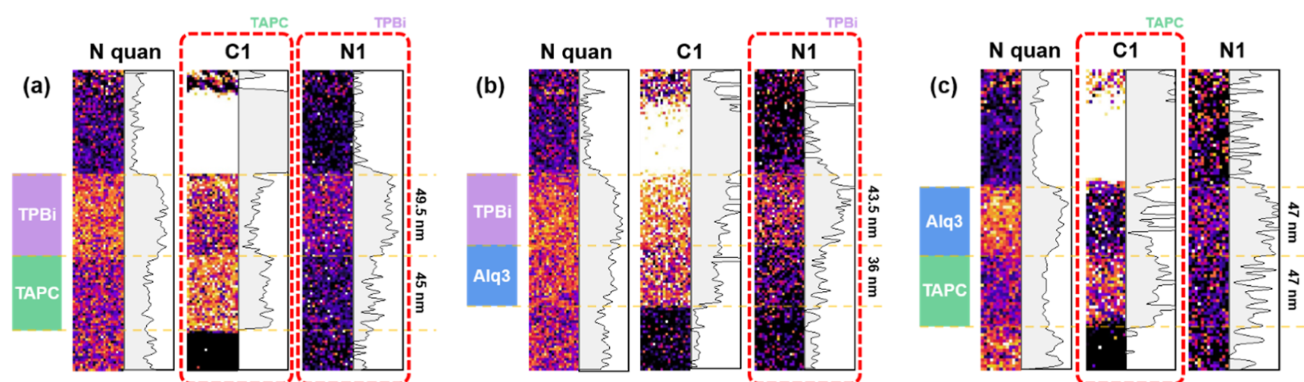

Figure 4. Mapping results of nitrogen components, aromatic carbon (C1), and pyridinic nitrogen (N1) for bilayer structures: (a) TPBi/TAPC, (b) TPBi/Alq3, and (c) Alq3/TAPC. The intensity profiles shown alongside the maps assist in layer separtion.

clearly observed at 398 and 399 eV, respectively, whereas the N1 peak was not detected in the case of Alq3. The characteristic bonding information on TPBi can be extracted from the pyridinic nitrogen bonding (N1 in Figure 3).[24,25] Results of the univocity N1 signal of TPBi indicate that the pyridinic bond only exists for TPBi. All materials exhibited the signal intensity for the N2 peak and pi bonding for C−N, corresponding well with the fact that the three samples have double C═N bonds. At enhanced energy resolution, the C K edge exhibited subtle differences in the carbon bonding state of the organic materials (Figure S1). While the characteristic N K edge feature is identifiable without using an energy-selecting slit, achieving a higher SNR is crucial for detecting lower nitrogen contents (Figure S2). Despite this limitation, the N K edge spectra provided distinct peaks for the three organic films. This suggests that FIB damage to the organic materials is negligible. Consequently, EELS can effectively differentiate between organic multilayers and measure the exact thickness of the films by spatially resolving the characteristic spectral peaks.

To visualize the bilayer OLED films using the monochromated LNES method, SI was conducted, which allowed us to obtain a high degree of spatial and energy resolution for the cross-sectional area.[26] Figure 4a−c shows the nitrogen quantification map, aromaticity of the benzenoid carbon from the C1 peak, and pyridinic nitrogen bond from the N1 peak, respectively. First, nitrogen was quantified using a linear fitting model of Hartree−Slater atomic simulated edges, which provided relatively high accuracy and reliability.[27,28] The nitrogen content obtained from mono-EELS is shown in Figure 4a; the thickness of TPBi was 49.5 nm. In addition, the figure shows an OLED thin film distinct from TAPC (45 nm). However, Alq3 and TAPC with different N contents exhibited the same trends as those of TPBi and TAPC, confirming that each OLED layer had a thickness of 47 nm.

We attempted spatial mapping from the C K/N K edge differentiated by mono-EELS in Figure 3. The C1 mapping results show a more prominent intensity for the TAPC film than for the other two materials (Figure 4a−c), indicating that pi bonding from the aromatic carbon ring is well-distributed over the TAPC film. Interestingly, the thickness of each OLED thin film was consistent with the nitrogen quantitative analysis results. The C1 mapping for TPBi and Alq3 in Figure 4b is inadequate for differentiating the bilayer structures because of their similar aromaticity. Therefore, we applied N1 mapping in this case, and the results highlighted that the pyridinic nitrogen bond of the TPBi film was stronger than that of the Alq3 film (Figure 4b). TPBi/TAPC, TPBi, and Alq3 could be effectively distinguished through SI mapping of the N1 peak. Therefore, monochromated ELNES mapping of the carbon and nitrogen chemical bonding states is very effective for observing the OLED bilayer at the nanometer scale. The thickness agreement between the quantification and bonding mapping provides credibility to these techniques. Furthermore, based on this EELS mapping data, more accurate etching rate and mass spectrometry data can be obtained by modifying the ToF-SIMS depth profiles measured previously.

■ CONCLUSIONS

In this study, we used monochromated EELS to analyze bilayered OLED thin films containing TAPC, TPBi, and Alq3. Advancements in the higher energy resolution of mono-EELS and detection efficiency have enabled the accurate measurement of spectral features at the C K and N K edges, specifically identifying aromatic carbon and pyridinic nitrogen in organic materials. When integrated with ToF-SIMS analysis, ELNES mapping effectively discerned unique chemical bonds, highlighting the contrasting molecular structures inherent within organic materials. This comprehensive approach allowed the visualization of bilayer thin films on the nanometer scale. Integrating monochromatic EELS with mass spectrometry demonstrated that microscopic analysis of OLED thin films would be particularly useful for the study of organic semiconductor materials such as OLEDs, organic photovoltaics, and organic thin-film transistors. Our work demonstrates the transformative prospects of combining high-resolution electron beams with a deep understanding of chemical bonds through mass spectrometry in devices featuring OLED materials.

■ ASSOCIATED CONTENT

Supporting Information

The Supporting Information is available free of charge at https://pubs.acs.org/doi/10.1021/acs.analchem.4c00742.

Monochromated and conventional C K and N K edges, effect of monochromation, energy resolution profiles, electron beam intensity profiles, and EELS measurement results (PDF)

■ AUTHOR INFORMATION

Corresponding Authors

Chang Min Choi − *Center for Scientific Instrumentation, Korea Basic Science Institute, Cheongju 28119, Republic of*

https://doi.org/10.1021/acs.analchem.4c00742
Anal. Chem. 2024, 96, 12616−12621

Korea; orcid.org/0000-0001-7708-9056;
Email: cmchoi@kbsi.re.kr

Jae Hyuck Jang – *Center for Research Equipment, Korea Basic Science Institute, Daejeon 34133, Republic of Korea; Graduate School of Analysis Science and Technology, Chungnam National University, Daejeon 34134, Republic of Korea;* orcid.org/0000-0002-9133-3286;
Email: jhjang@kbsi.re.kr

Authors

Kyun Seong Dae – *Center for Research Equipment, Korea Basic Science Institute, Daejeon 34133, Republic of Korea*

Kyoung-Soon Jang – *Center for Research Equipment, Korea Basic Science Institute, Daejeon 34133, Republic of Korea*

Complete contact information is available at:
https://pubs.acs.org/10.1021/acs.analchem.4c00742

Author Contributions

[‖]C.M.C. and J.H.J. are cocorresponding authors who contributed equally. The manuscript was written through contributions of all authors. All authors have given approval to the final version of the manuscript.

Notes

The authors declare no competing financial interest.

■ ACKNOWLEDGMENTS

This study was supported by a research grant from the Korea Basic Science Institute (D411000) and a National Research Foundation of Korea (NRF) grant funded by the Korean Government (MSIT) (no. 2020R1C1C100521913). J.H.J. was also supported by the Technology Innovation Program (20010542), funded by MOTIE, Korea.

■ REFERENCES

(1) Tang, C. W.; Vanslyke, S. A. *Appl. Phys. Lett.* **1987**, *51*, 913–915.
(2) Burroughes, J. H.; Bradley, D. D. C.; Brown, A. R.; Marks, R. N.; Mackay, K.; Friend, R. H.; Burns, P. L.; Holmes, A. B. *Nature* **1990**, *347* (6293), 539–541.
(3) D'Andrade, B. W.; Forrest, S. R. *Adv. Mater.* **2004**, *16* (18), 1585–1595.
(4) Schwartz, G.; Reineke, S.; Rosenow, T. C.; Walzer, K.; Leo, K. *Adv. Funct. Mater.* **2009**, *19* (9), 1319–1333.
(5) Jiang, X.; Liu, Y.; Song, X.; Zhu, D. *Solid State Commun.* **1996**, *99* (3), 183–187.
(6) Jordan, R. H.; Dodabalapur, A.; Strukelj, M.; Miller, T. M. *Appl. Phys. Lett.* **1996**, *68* (9), 1192–1194.
(7) D'Andrade, B. W.; Brooks, J.; Adamovich, V.; Thompson, M. E.; Forrest, S. R. *Adv. Mater.* **2002**, *14* (15), 1032–1036.
(8) Zugang, L.; Nazarè, H. *Synth. Met.* **2000**, *111–112*, 47–51.
(9) Meerheim, R.; Lussem, B.; Leo, K. *Proc. IEEE* **2009**, *97* (9), 1606–1626.
(10) Lee, J.; Chen, H. F.; Batagoda, T.; Coburn, C.; Djurovich, P. I.; Thompson, M. E.; Forrest, S. R. *Nat. Mater.* **2016**, *15* (1), 92–98.
(11) Kuei, C. Y.; Tsai, W. L.; Tong, B.; Jiao, M.; Lee, W. K.; Chi, Y.; Wu, C. C.; Liu, S. H.; Lee, G. H.; Chou, P. T. *Adv. Mater.* **2016**, *28* (14), 2795–2800.
(12) Zou, S. J.; Shen, Y.; Xie, F. M.; Chen, J. D.; Li, Y. Q.; Tang, J. X. *Mater. Chem. Front.* **2020**, *4* (3), 788–820.
(13) Iida, S.-i.; Murakami, T.; Kurosawa, Y.; Suzuri, Y.; Fisher, G. L.; Miyayama, T. *Rapid Commun. Mass Spectrom.* **2020**, *34* (7), No. e8640.
(14) Graff, A.; Altmann, F.; Dzwilewski, A.; Freitag, B. *Microsc. Microanal.* **2014**, *20* (S3), 144–145.
(15) Höfle, S.; Bernhard, C.; Bruns, M.; Kübel, C.; Scherer, T.; Lemmer, U.; Colsmann, A. *ACS Appl. Mater. Interfaces* **2015**, *7* (15), 8132–8137.
(16) Juhl, S.; Li, X.; Badding, J.; Alem, N. *Microsc. Microanal.* **2016**, *22* (S3), 1840–1841.
(17) Juhl, S. J.; Wang, T.; Vermilyea, B.; Li, X.; Crespi, V. H.; Badding, J. V.; Alem, N. *J. Am. Chem. Soc.* **2019**, *141* (17), 6937–6945.
(18) Huang, H.-T.; Ward, M. D.; Juhl, S. J.; Biswas, A.; Alem, N.; Badding, J. V.; Strobel, T. A. *Microsc. Microanal.* **2018**, *24* (S1), 2030–2031.
(19) Spillane, L.; Longo, P.; Schaffer, B.; Miller, B.; Thomas, P.; Twesten, R. *Microsc. Microanal.* **2020**, *26* (S2), 1676–1677.
(20) Baek, J. Y.; Choi, C. M.; Lee, S. J.; Min, B. K.; Kang, H. S.; Choo, D. C.; Sung, J. Y.; Jin, J. S.; Choi, M. C. *Appl. Surf. Sci.* **2020**, *507* (November 2019), 144887.
(21) Sedlmair, J.; Gleber, S. C.; Peth, C.; Mann, K.; Niemeyer, J.; Thieme, J. *J. Soils Sediments* **2012**, *12* (1), 24–34.
(22) Wang, B.; Wang, Z. K.; Liang, J.; Li, M.; Hu, Y.; Liao, L. S. *J. Mater. Chem. C* **2017**, *5* (41), 10721–10727.
(23) Solomon, D.; Lehmann, J.; Kinyangi, J.; Liang, B.; Heymann, K.; Dathe, L.; Hanley, K.; Wirick, S.; Jacobsen, C. *Soil Sci. Soc. Am. J.* **2009**, *73* (6), 1817–1830.
(24) Kiuchi, H.; Kondo, T.; Sakurai, M.; Guo, D.; Nakamura, J.; Niwa, H.; Miyawaki, J.; Kawai, M.; Oshima, M.; Harada, Y. *Phys. Chem. Chem. Phys.* **2016**, *18* (1), 458–465.
(25) Matter, P. H.; Zhang, L.; Ozkan, U. S. *J. Catal.* **2006**, *239* (1), 83–96.
(26) Kimoto, K.; Asaka, T.; Nagai, T.; Saito, M.; Matsui, Y.; Ishizuka, K. *Nature* **2007**, *450* (7170), 702–704.
(27) Hunt, J. A.; Williams, D. B. *Ultramicroscopy* **1991**, *38* (1), 47–73.
(28) Manoubi, T.; Tencé, M.; Walls, M. G.; Colliex, C. *Microsc., Microanal., Microstruct.* **1990**, *1* (1), 23–39.

https://doi.org/10.1021/acs.analchem.4c00742
Anal. Chem. 2024, 96, 12616–12621